

Geophysical Research Letters

RESEARCH LETTER

10.1029/2020GL090973

Key Points:

- Water content in hydrous silicate melt decreases with increasing temperature
- Water content in hydrous melt is relatively independent of chemical composition and coexisting phases
- The dehydration melt at 660-km depth contains 20–50 wt.% depending on temperature conditions

Supporting Information:

- Supporting Information S1

Correspondence:

H. Fei,
hongzhan.fe@uni-bayreuth.de

Citation:

Fei, H. (2021). Water content of the dehydration melting layer in the topmost lower mantle. *Geophysical Research Letters*, 48, e2020GL090973. <https://doi.org/10.1029/2020GL090973>

Received 25 SEP 2020
 Accepted 18 NOV 2020

© 2020. The Authors.
 This is an open access article under the terms of the [Creative Commons Attribution](https://creativecommons.org/licenses/by/4.0/) License, which permits use, distribution and reproduction in any medium, provided the original work is properly cited.

Water Content of the Dehydration Melting Layer in the Topmost Lower Mantle

Hongzhan Fei¹ 

¹Bayerisches Geoinstitut, University of Bayreuth, Bayreuth, Germany

Abstract The water-rich mantle transition zone and dry lower mantle suggest that a dehydration melting layer can form at the 660-km depth boundary. However, the water content of the melting layer ($C_{\text{H}_2\text{O}}^{\text{melt}}$), which dominates its gravitational stability and melt fraction, remains poorly constrained. Here, the $C_{\text{H}_2\text{O}}^{\text{melt}}$ of hydrous silicate melt by mass balance calculations is investigated and found that $C_{\text{H}_2\text{O}}^{\text{melt}}$ significantly decreases with increasing temperature, but is relatively insensitive to chemical composition (FeO and SiO₂ contents) and coexisting phases. Melt at 660-km depth should contain ~50 wt.% water at 1600 K (slab geotherm) or ~20 wt.% water at 2000 K (topmost lower mantle geotherm). The density of the hydrous melt is <3.9 g/cm³, which makes it buoyant. With a melt fraction of ≥ 0.5 vol.%, the melting layer is expected to significantly reduce the viscosity and seismic velocity near slabs, which may cause slab stagnation and prohibit whole mantle convection.

Plain Language Summary A dehydration melting layer is predicted near the 660-km depth boundary by the phase transition of hydrous ringwoodite in the mantle transition zone to dry bridgmanite and ferropericlase in the lower mantle. However, the water content in the melt, which controls the melt density and thus gravitational stability, remains poorly constrained. In this study, the water content in hydrous melt under 660-km depth conditions is estimated as a function of temperature. At 2000 K, corresponding to topmost lower mantle geotherm, hydrous silicate melt should contain ~20 wt.% water, which will cause the melt to be gravitationally unstable. The melt fraction at 660-km depth is estimated to be >0.5 vol.%, which may significantly reduce rock viscosity and seismic velocity.

1. Introduction

The mantle transition zone is considered to be a water reservoir because its dominant minerals, wadsleyite, and ringwoodite, contain up to ~1.0 wt.% based on several lines of evidence, including electrical conductivity (Kelbert et al., 2009), mineral viscosity (Fei et al., 2017), and naturally formed water-rich ringwoodite inclusion (Pearson et al., 2014). In contrast, the lower mantle is considered to be dry (Hirschmann, 2006) because bridgmanite and ferropericlase can contain ≤ 0.1 wt.% water in their crystal structures (e.g., Bolfan-Casanova et al., 2000; Fu et al., 2019). Dehydration melting should therefore occur during the phase transformation of hydrous ringwoodite to bridgmanite and ferropericlase by mass convection when crossing the 660-km boundary (Schmandt et al., 2014). Such a dehydration melting layer has been interpreted to explain the seismic velocity reduction at the topmost lower mantle (Schmandt et al., 2014).

The question arises regarding whether this melting layer is stabilized at 660-km depth or gravitationally unstable. This problem should be determined by the melt viscosity, wetting of mineral grain-boundaries, and most importantly density because the density contrast among the transition zone, lower mantle, and hydrous melt is the driving force for upward or downward melt migration. Melt density is known to decrease with increasing $C_{\text{H}_2\text{O}}^{\text{melt}}$ (e.g., Matsukage et al., 2005; Sakamaki et al., 2006). Therefore, although dry melt [4.0–4.4 g/cm³ after correction to 23 GPa and 1600–2000 K (Bajgain et al., 2015; Ohtani & Maeda, 2001; Sanloup et al., 2013)] is denser than the mantle transition zone [3.9–4.0 g/cm³ (Dziewonski & Anderson, 1981)], hydrous melt could be either comparable or less dense depending on its $C_{\text{H}_2\text{O}}^{\text{melt}}$. Understanding $C_{\text{H}_2\text{O}}^{\text{melt}}$ at 660-km depth is therefore essential for evaluating its density and stability.

Nakajima et al. (2019) reported $C_{\text{H}_2\text{O}}^{\text{melt}} \approx 30$ wt.% at 660-km depth conditions and no clear temperature effect. However, $C_{\text{H}_2\text{O}}^{\text{melt}}$ is difficult to calculate precisely using mass balance owing to the small melt fractions in their samples. Their $C_{\text{H}_2\text{O}}^{\text{melt}}$ values were obtained as the deviation from 100% of the total weight percent in the energy dispersive spectrometry analysis, which may contain large uncertainties because the weight percent of quenched melt is correlated not only with $C_{\text{H}_2\text{O}}^{\text{melt}}$ but also porosity and $\text{Fe}^{3+}/\Sigma\text{Fe}$, both of which are highly uncertain. Additionally, the compositional dependence of $C_{\text{H}_2\text{O}}^{\text{melt}}$ is also unclear.

In this study, $C_{\text{H}_2\text{O}}^{\text{melt}}$ of hydrous silicate melt using multi-anvil experiments at 1600–2300 K and 23–23.5 GPa by mass balance calculation was estimated. To minimize experimental uncertainty, samples with a simple system (MgO-SiO₂-H₂O-FeO) and high melt fraction (>20 vol.%) were used; the melt consequently coexists with minimized solid phases (majorly ringwoodite and bridgmanite). The results indicate that $C_{\text{H}_2\text{O}}^{\text{melt}}$ systematically decreases with increasing temperature, but is relatively insensitive to FeO and SiO₂ contents and coexisting phases.

2. Methods

2.1. High-Pressure Experiments

Mixtures with bulk compositions of (Mg,Fe)₂SiO₄ and (Mg,Fe)SiO₃ plus 5–22 wt.% H₂O (Table 1) were prepared from MgO, SiO₂, Mg(OH)₂, and FeO powders. After drying in a vacuum furnace at 400 K, the mixtures were sealed in Pt-Rh or Pt capsules by arc-welding (Fei & Katsura, 2020). The inner and outer diameters (ID/OD) of the Pt-Rh capsules were 1.0/1.2 mm for the 23 GPa runs, whereas Pt capsules with ID/OD = 0.8/1.0 mm were used for the 23.5 GPa runs. The high-pressure experiments were performed using a Kawai-type multi-anvil apparatus with standard 10/4 and 7/3 cell assemblies at the Bayerisches Geoinstitut (supporting information). The experimental temperatures ranged between 1600 and 2300 K, measured by a D-type (W/Re) thermocouple, with annealing durations of 5–1800 min (Table 1).

Cross sections parallel to the axial directions of the capsules were prepared by polishing with sandpaper and diamond powder. The run products appear as coexisting crystals (majorly bridgmanite and ringwoodite) and quenched crystallized melts (Table 1), as confirmed by scanning electron microscope (SEM) and microfocus X-ray diffraction analyses (Figure 1). The compositions of the melts were analyzed by electron microprobe (EPMA) operated with an acceleration voltage of 15 kV, beam current of 15 nA, beam size of 30–50 μm, and counting time of 20 s. The (Mg + Fe)/Si and Fe/(Fe + Mg) atomic ratios in the melts, which reflect the SiO₂ and FeO concentrations, respectively, were calculated from the EPMA data (supporting information).

2.2. Melt Fraction and $C_{\text{H}_2\text{O}}^{\text{melt}}$ Estimation

The melt and solid fractions were obtained from the SEM images using image processing software (ImageJ). Images of all recovered capsules are provided in the supporting information. The $C_{\text{H}_2\text{O}}^{\text{melt}}$ values were calculated by mass balance using the initial bulk water content in the starting materials, water content in ringwoodite (Fei & Katsura, 2020), and fractions of melts and solids. The water content in bridgmanite (and akimotoite) is negligible in comparison with ringwoodite and melt (Bolfan-Casanova et al., 2000; Fu et al., 2019) and therefore has a negligible effect on $C_{\text{H}_2\text{O}}^{\text{melt}}$, although the water solubility in bridgmanite remains under debate (e.g., Fu et al., 2019; Litasov et al., 2002).

2.3. Experimental Uncertainty Evaluation

A critical assumption in the above mass balance calculation is no water loss during the experiments. To examine if this assumption is reasonable or not, information regarding how the bulk water content in the capsule changes with time is required. A time series was therefore performed under the same pressure and temperature conditions (23 GPa, 2000 K) with the same starting material (Fo₉₀ + 15%H₂O), but different durations (5–1800 min). The melt fraction in the run products, which is controlled by the bulk water content,

Table 1
List of Run Conditions, Melt Fractions, $C_{H_2O}^{melt}$, and Characterization of the Run Products

Starting material	Bulk composition ^a	Bulk H ₂ O content (%)	Run. No.	T (K)	P (GPa)	t (min)	Phases	Melt fraction (vol.%)	$C_{H_2O}^{melt}$ (wt.%)	C_{H_2O} in Rw ^c (wt.%)	H ₂ O partition coefficient (melt/rw.)	Fe/(Mg + Fe) in melt	(Mg + Fe)/Si in melt
Fo ₁₀₀ + 5%H ₂ O	100(Mg ₂ SiO ₄) + 5H ₂ O	4.76	H4775	2000	23	300	Rw + melt	20.3	21.4	0.53	40.3	0	2.35(18)
Fo ₁₀₀ + 15%H ₂ O	100(Mg ₂ SiO ₄) + 15H ₂ O	13.04	H4805	2000	23	300	Rw + melt	57.0	22.2	0.95	23.3	0	1.89(5)
Fo ₉₀ + 5%H ₂ O	100(Mg _{1.8} Fe _{0.2} SiO ₄) + 5H ₂ O	4.76	H4784H	1800	23	300	Rw + Aki + melt	46.0	26.5	1.90	13.9	0	2.39(19)
Fo ₉₀ + 15%H ₂ O	100(Mg _{1.8} Fe _{0.2} SiO ₄) + 15H ₂ O	13.04	H4711	2000	23	240	Rw + Aki + melt	24.6	18.3	0.33	55.6	18.4(7)%	1.98(9)
(Fo ₉₀ + 15%H ₂ O) + En ₉₀	100(Mg _{1.8} Fe _{0.2} SiO ₄) + 15H ₂ O + 115(Mg _{0.9} Fe _{0.1} SiO ₃)	6.56	H4698	2000	23	120	Rw + Aki + melt	69.5	18.3	1.03	17.8	12.9(2)%	1.96(5)
			S7011	2000	23	180	Rw + Aki + melt	68.3	18.7	1.00	18.8	12.6(4)%	2.10(8)
			S7504	2000	23	5	Rw + Aki + melt	55.3	22.8	0.92	24.8	13.8(3)%	1.96(6)
			S7505	2000	23	1800	Rw + Aki + melt	58.6	21.7	0.88	24.7	14.5(4)%	2.09(2)
			H4723	1800	23	180	Rw + Aki + melt	45.6	28.0	1.13	24.7	15.8(3)%	2.50(11)
			H4720	1600	23	300	Rw + Aki + melt + st	23.3	52.4	1.30	40.4	20.7(5)%	3.20(11)
(Fo ₉₀ + 15%H ₂ O) + En ₉₀	100(Mg _{1.8} Fe _{0.2} SiO ₄) + 15H ₂ O + 115(Mg _{0.9} Fe _{0.1} SiO ₃)	6.56	H4891	2000	23.5	120	Bdg + Rw + melt	30.0	21.0	0.93	22.5	19.5(4)%	3.14(6)
2(Fo ₉₀ + 15%H ₂ O) + En ₉₀	200(Mg _{1.8} Fe _{0.2} SiO ₄) + 30H ₂ O + 115(Mg _{0.9} Fe _{0.1} SiO ₃)	8.70	H4896	2300 ^b	23.5	120	Bdg + melt	74.7	11.6	-	-	11.6(6)%	1.94(10)
Fo ₉₀ + 22%H ₂ O	100(Mg _{1.8} Fe _{0.2} SiO ₄) + 22H ₂ O	18.03	S7051	2000	23	240	Rw + Aki + melt	84.4	21.2	0.96	22.1	10.9(5)%	2.08(6)
Fo ₇₅ + 15%H ₂ O	100(Mg _{1.3} Fe _{0.5} SiO ₄) + 15H ₂ O	13.04	H4762	2000	23	300	Rw + melt + st	70.9	18.0	1.00	18.1	31.6(8)%	2.43(7)
2(Fo ₇₅ + 15%H ₂ O) + En ₉₀	200(Mg _{1.3} Fe _{0.5} SiO ₄) + 30H ₂ O + 115(Mg _{0.9} Fe _{0.1} SiO ₃)	8.70	H4961	2000	23.5	20	Bdg + melt + st	51.1	17.0	-	-	21.3(6)%	2.29(10)

Note. Bdg, bridgmanite; Rw, ringwoodite; Aki, akimotoite; St, stishovite; Fo₁₀₀, Mg₂SiO₄; Fo₉₀, Mg_{1.8}Fe_{0.2}SiO₄; Fo₇₅, Mg_{1.3}Fe_{0.5}SiO₄; En₉₀, Mg_{0.9}Fe_{0.1}SiO₃.

^aThe starting materials are mixtures of MgO, SiO₂, FeO, and Mg(OH)₂ with a bulk composition of 100 wt.% silicate plus 5–22 wt.% H₂O. The number of each component in this column indicates the weight ratio. For example, 100(Mg₂SiO₄) + 5H₂O means that the weight ratio of Mg₂SiO₄ and H₂O is 100:5 and is therefore named Fo₁₀₀ + 5%H₂O with bulk water content of 5/(100 + 5) = 4.76%. ^bThe temperature in this run is estimated from the power-temperature relationship. ^cThe C_{H_2O} in ringwoodite data are reported in Fei and Katsura (2020).

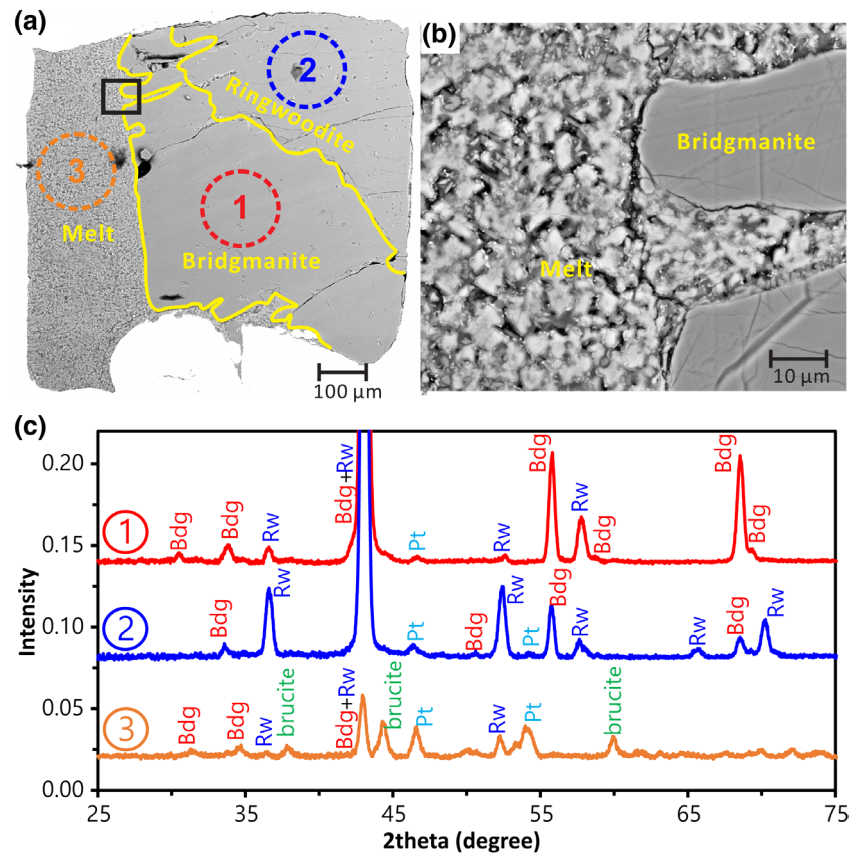


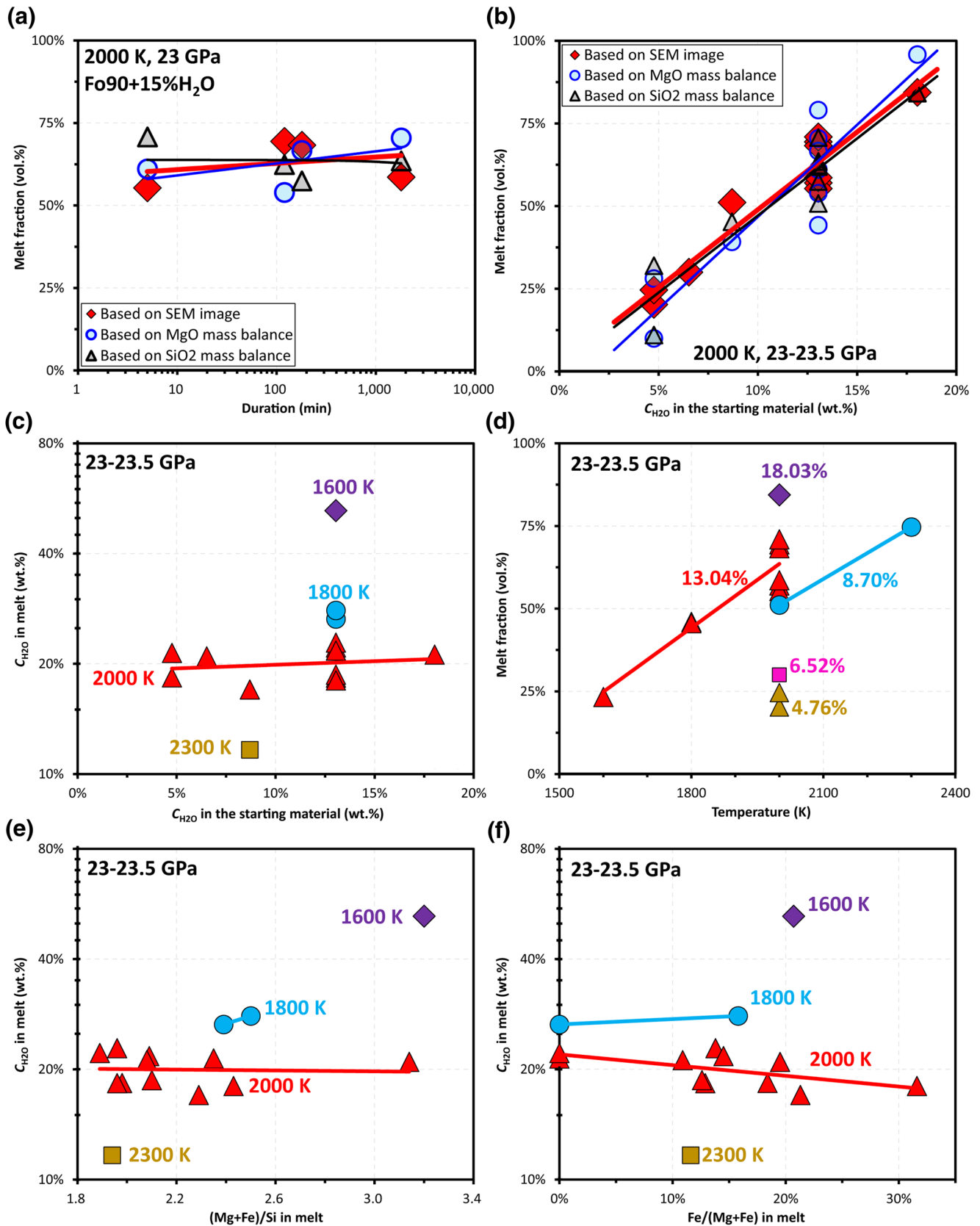
Figure 1. Characterization of run product (H4891). (a) Backscattered electron image of the whole capsule. (b) Quenched structure of the melt in the rectangular area in (a). (c) X-ray diffraction of different regions in (a). Brucite peaks are found in the melt, which should have formed by crystallization during quenching, whereas the Pt peak is from the sample capsule due to the limited spatial resolution of the X-ray diffractometer. Bdg: bridgmanite. Rw: ringwoodite.

is found to be independent of duration (Figure 2a), which indicates that water loss was insignificant. This is understandable because hydrogen may diffuse through Pt capsule walls in the form of H_2 , but not as hydroxyl or H_2O (e.g., Eugster, 1957; Shaw, 1963), which is the case in this study. Although H_2O could be partially reduced to H_2 by Fe^{2+} in the Fe-bearing runs, even if all the Fe^{2+} were oxidized to Fe^{3+} , the amount of H_2O reduced to H_2 would be very small (e.g., the bulk water content would decrease from 13.0% to 12.1% in the $FO_{90} + 15\%H_2O$ system).

Some may consider that a time series over a duration of 5–1,800 min does not indicate the extent water loss during the initial 5 min. However, if water loss had occurred, the loss rate should be controlled by the water fugacity contrast in and out of the capsule. As far as the melt phase presents, the water fugacity is constant and the loss rate should thus be constant. Therefore, if water loss were significant within the first 5 min, the melt phase should not be present over long-duration runs, which is clearly not the case in this study.

Another error source is the uncertainty of the melt fraction estimation. To minimize this uncertainty, (i) all capsules were polished to nearly the center; therefore, the melt fraction in the cross section most likely represents the entire capsule; (ii) only runs with high melt fractions ($\geq 20\%$) were used; and (iii) the melt fractions based on SEM images were independently examined by mass balance calculations of MgO and SiO_2 concentrations in the solids and melts (Tables S1 and S2). As shown in Figures 2a and 2b, the melt fractions estimated by different methods follow the same trend and agree well with each other. The uncertainty of the melt fraction estimation is therefore limited.

Additional potential error sources include the following: (i) Uncertainty of the water content in solid phases. This should be negligible because the majority of water ($>90\%$) within the capsule is stored by melt.



(ii) Water gain during sample preparation. The sample powder may absorb moisture from the air, but this amount ($\ll 0.5$ wt.%) is small in comparison with the bulk $C_{\text{H}_2\text{O}}$ in the starting materials. (iii) Pressure and temperature uncertainties. The appearance of both Fe-free and Fe-bearing ringwoodite at 2000 K and the coexistence of ringwoodite and bridgmanite in H4891 indicate a pressure uncertainty of less than 1.5 GPa (Presnall, 1995). The temperature gradient in a typical multi-anvil experiment is ~ 100 K/mm (Hernlund et al., 2006). Considering the capsule lengths of 1.2–1.3 mm located at the center, the temperature uncertainty in this study should be less than 70 K. Because the magnitude of each error source is unknown, it is impossible to quantitatively evaluate the error bar for each data point. Nevertheless, the systematic variation of $C_{\text{H}_2\text{O}}^{\text{melt}}$ with temperature and reproducible $C_{\text{H}_2\text{O}}^{\text{melt}}$ from different runs demonstrate that the uncertainty of $C_{\text{H}_2\text{O}}^{\text{melt}}$ is relatively small, which should be within the scatter range of the data points.

3. Melt Fraction and $C_{\text{H}_2\text{O}}^{\text{melt}}$ in the Run Products

The $C_{\text{H}_2\text{O}}^{\text{melt}}$ values based on mass balance calculations do not show a clear correlation with the total mass from the EPMA analysis (supporting information), which is not surprising because, as explained in Section 1, the $C_{\text{H}_2\text{O}}^{\text{melt}}$ estimated from the EPMA analysis is likely highly uncertain. Therefore, the melt fraction and $C_{\text{H}_2\text{O}}^{\text{melt}}$ based on mass balance calculation are plotted in Figure 2 as functions of run duration (Figure 2a), starting material (Figures 2b and 2c), temperature (Figure 2d), and melt composition (Figures 2e and 2f). The melt fraction increases with increasing initial water content in the starting material, but $C_{\text{H}_2\text{O}}^{\text{melt}}$ remains unchanged (Figures 2b–2d). This is reasonable because the water partition coefficient between melt and solid should be constant at a given temperature. As shown in Table 1, the partition coefficient is nearly constant (18–25) at 2000 K even with various starting compositions (except runs H4711 and H4775, in which ringwoodite has a lower water content than the other runs because of different SiO_2 -activity conditions [Fei & Katsura, 2020]).

$C_{\text{H}_2\text{O}}^{\text{melt}}$ clearly decreases with increasing temperature, but shows no meaningful dependence of $(\text{Mg} + \text{Fe})/\text{Si}$ and $\text{Fe}/(\text{Mg} + \text{Fe})$ ratios (Figures 2c, 2e, and 2f). Additionally, although the melt coexists with various solid phases in the run products (Table 1), the $C_{\text{H}_2\text{O}}^{\text{melt}}$ values do not show a clear difference. It is thus concluded that $C_{\text{H}_2\text{O}}^{\text{melt}}$ has strong temperature dependence, but is relatively insensitive to chemical composition, coexisting phases, and bulk water content in the system. Therefore, even though experiments in this study were performed with a simple system ($\text{MgO-SiO}_2\text{-FeO-H}_2\text{O}$) and high bulk water content, they should still be able to represent $C_{\text{H}_2\text{O}}^{\text{melt}}$ in the lower mantle.

4. Temperature Dependence of $C_{\text{H}_2\text{O}}^{\text{melt}}$

As shown in Figure 3, $C_{\text{H}_2\text{O}}^{\text{melt}}$ systematically decreases from 52 to 12 wt.% with increasing temperature from 1600 to 2300 K. The absolute values of $C_{\text{H}_2\text{O}}^{\text{melt}}$ are basically consistent with that of 29.9 ± 4.1 wt.% reported by Nakajima et al. (2019) (Figure 3). However, their experimental temperature range was relatively small (1570–1870 K), which may mask the temperature dependence.

The $C_{\text{H}_2\text{O}}^{\text{melt}}$ determined in this study apparently follows an exponential function of reciprocal temperature ($1/T$). The data points are thus fitted to the equation,

$$C_{\text{H}_2\text{O}}^{\text{melt}} = C_0 \exp\left(-\frac{\Delta G}{RT}\right) \quad (1)$$

Figure 2. Melt fraction and $C_{\text{H}_2\text{O}}^{\text{melt}}$ in the run products. (a) Melt fraction is independent from run duration, indicating no significant water loss during the experiments. (b) Melt fraction increases with increasing bulk $C_{\text{H}_2\text{O}}$ in the starting material. Melt fraction estimated from the SEM images is consistent with that based on MgO and SiO_2 mass balance calculations. (c) $C_{\text{H}_2\text{O}}^{\text{melt}}$ is independent of bulk $C_{\text{H}_2\text{O}}$ in the starting material. (d) Melt fraction is correlated to the experimental temperature. Numbers next to the data points represent the bulk $C_{\text{H}_2\text{O}}$ in the starting material. (e) $C_{\text{H}_2\text{O}}^{\text{melt}}$ is independent of the $(\text{Mg} + \text{Fe})/\text{Si}$ ratio. (f) $C_{\text{H}_2\text{O}}^{\text{melt}}$ is relatively insensitive to the $\text{Fe}/(\text{Mg} + \text{Fe})$ ratio.

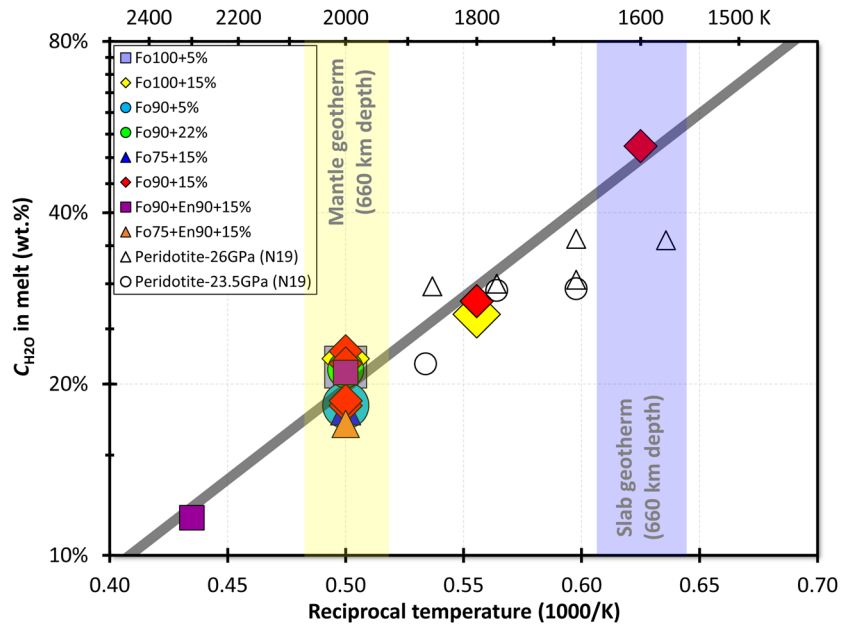


Figure 3. $C_{\text{H}_2\text{O}}^{\text{melt}}$ as a function of temperature at 23–23.5 GPa. Different symbols represent results from different starting materials, as listed in Table 1. The data by N19 (Nakajima et al., 2019) with peridotite + H_2O as starting material are also shown for comparison.

where $C_{\text{H}_2\text{O}}^{\text{melt}}$ is the water content in wt.%, T is the temperature, R is the ideal gas constant, C_0 is a constant, and ΔG is the chemical potential difference of H_2O between melt and solid. By least square fitting, the C_0 and ΔG are found to be $10^{-0.32 \pm 0.17}$ and -61.5 ± 5.3 kJ/mol, respectively.

In the view of thermodynamics, the chemical potential of H_2O in solid ($\mu_{\text{H}_2\text{O}}^{\text{solid}}$) and melt ($\mu_{\text{H}_2\text{O}}^{\text{melt}}$) phase is as follows:

$$\mu_{\text{H}_2\text{O}}^{\text{solid}} = \mu_{\text{H}_2\text{O}}^{\text{0solid}} + RT \ln(a_{\text{H}_2\text{O}}^{\text{solid}}) \quad (2)$$

$$\mu_{\text{H}_2\text{O}}^{\text{melt}} = \mu_{\text{H}_2\text{O}}^{\text{0melt}} + RT \ln(a_{\text{H}_2\text{O}}^{\text{melt}}) \quad (3)$$

where μ^0 is the standard chemical potential of H_2O in the hypothetical endmember and a is the activity of H_2O in the solid or melt phases.

Under equilibrium, we have $\mu_{\text{H}_2\text{O}}^{\text{solid}} = \mu_{\text{H}_2\text{O}}^{\text{melt}}$. By assuming an ideal mixing process for H_2O incorporation, the H_2O activity is identical to the concentration. Therefore,

$$c_{\text{H}_2\text{O}}^{\text{melt}} = c_{\text{H}_2\text{O}}^{\text{solid}} \exp\left(-\frac{\mu_{\text{H}_2\text{O}}^{\text{0melt}} - \mu_{\text{H}_2\text{O}}^{\text{0solid}}}{RT}\right) \quad (4)$$

Because the temperature dependence of $C_{\text{H}_2\text{O}}^{\text{solid}}$ is relatively small in comparison with $C_{\text{H}_2\text{O}}^{\text{melt}}$ (Fei & Katsura, 2020), $C_{\text{H}_2\text{O}}^{\text{melt}}$ apparently becomes an exponential function of $1/T$.

5. Stability of the Melting Layer at 660-km Depth

A dehydration melting layer caused by downwelling flow (e.g., subducted slabs) is seismically interpreted at the topmost lower mantle near the 660-km discontinuity (Schmandt et al., 2014). The gravitational stability of this melting layer should be dominated by the melt density and therefore controlled by $C_{\text{H}_2\text{O}}^{\text{melt}}$ at

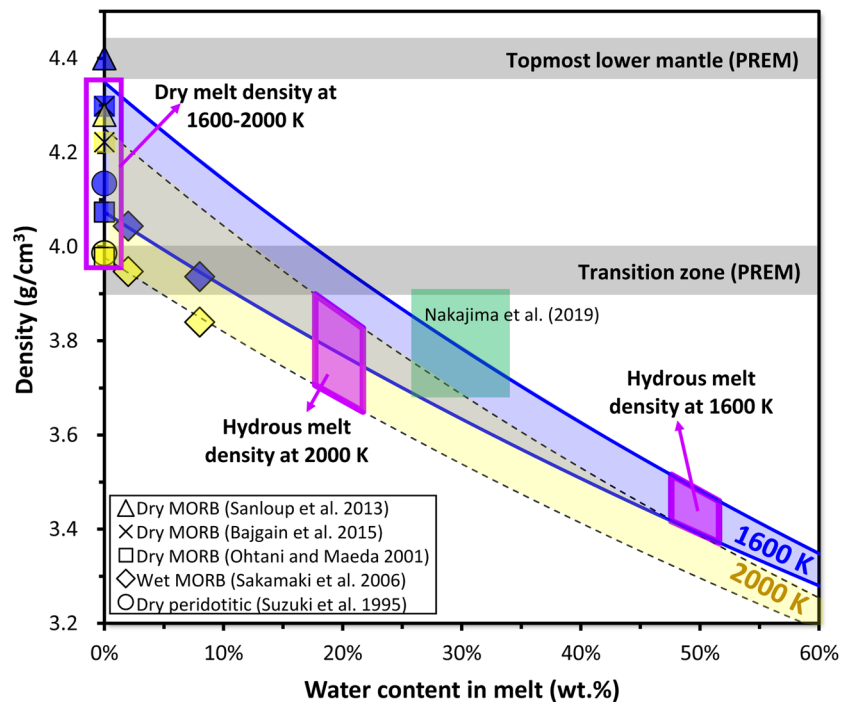


Figure 4. Density contrast of the transition zone, topmost lower mantle, and hydrous melt at 660-km depth. The blue and yellow regions are MORB melt density ranges at 1600 K (slab) and 2000 K (ambient mantle), respectively. The upper limit of each region is based on the dry MORB melt density given by Bajgain et al. (2015) and Sanloup et al. (2013). The lower limit is based on dry MORB and peridotitic melt given by Ohtani and Maeda (2001) and Suzuki et al. (1995), with a partial mole volume of 6.2–6.4 cm³/mol for H₂O at 23.5 GPa and 1600–2000 K (Sakamaki et al., 2006). All data are recalculated to 23.5 GPa and 1600 K (blue) or 2000 K (yellow) using their reported Birch-Murnaghan equation of state parameters and corresponding temperature dependences. PREM: density of the preliminary reference Earth model (Dziewonski & Anderson, 1981).

mantle temperatures. The geotherm of the topmost lower mantle is ~2000 K (Katsura et al., 2010), whereas the slabs are 300–500 K lower, that is, ~1600 K (Litasov et al., 2013; Tan et al., 2002). Sink/float experiments using multi-anvil techniques (Ohtani & Maeda, 2001; Sakamaki et al., 2006; Suzuki & Ohtani, 2003; Suzuki et al., 1995) suggest a melt density of 4.0 and 4.1 g/cm³ at 2000 and 1600 K, respectively, for both dry MORB and peridotitic melts after adjusting to 660-km depth pressure (~23.5 GPa). However, this value might be slightly underestimated because small amounts of water are always inevitable in multi-anvil experiments. On the other hand, first-principle simulations (Bajgain et al., 2015) and X-ray diffraction in diamond anvil cell experiments (Sanloup et al., 2013) indicate a dry MORB melt density of 4.2–4.4 g/cm³ at 1600–2000 K (Figure 4).

According to the results from this study, C_{H₂O}^{melt} is ~20 and 50 wt.% at 2000 and 1600 K, respectively. Using a H₂O partial mole volume of 6.2–6.4 cm³/mol in silicate melt (Sakamaki et al., 2006), the density of a hydrous melt with 20 wt.% water (2000 K) is estimated to be 3.7–3.9 g/cm³, and 3.4–3.5 g/cm³ for a melt with 50 wt.% water (1600 K). This is comparable with that reported by Nakajima et al. (2019) (3.6–3.9 g/cm³) at 23.5 GPa and 1570–1870 K, as shown in Figure 4. However, as explained previously, the absolute values of C_{H₂O}^{melt} as well as the temperature and composition dependences were not well constrained in Nakajima et al. (2019).

Although density may increase with Fe content (Matsukage et al., 2005), the FeO wt.% in hydrous peridotitic melt that coexists with bridgmanite is even lower than anhydrous melt (Ito & Takahashi, 1987; Nakajima et al., 2019). The hydrous melt at the topmost lower mantle is therefore always less dense than the transition zone. It should be maintained by downward flow and moves upward by buoyancy. By upwelling, ringwoodite with ~1 wt.% H₂O is expected to crystallize from the melt. Because C_{H₂O}^{melt} >> 1%, the excess water (melt) may continuously move upward and reach the 410-km discontinuity where hydrous melt may be gravitationally stable (Matsukage et al., 2005; Sakamaki et al., 2006).

6. Melt Fraction at the Topmost Lower Mantle

The melt fraction at the topmost lower mantle can be estimated from $C_{\text{H}_2\text{O}}^{\text{melt}}$ by a given water-content in the mantle transition zone. If we consider 55 vol.% ringwoodite in the mantle transition zone with ~ 1.0 wt.% water (e.g., Fei & Katsura, 2020; Fei et al., 2017; Pearson et al., 2014), using $C_{\text{H}_2\text{O}}^{\text{melt}} = 50$ wt.% at 1600 K determined in this study, the melt fraction in the topmost lower mantle is estimated to be 1.3 vol.% based on mass balance by assuming negligible water in ferropericlase and bridgmanite (Bolfan-Casanova, 2000; Fu et al., 2019). Even if using a relatively dry transition zone model (~ 0.4 wt.% water based on seismic velocity [Houser, 2016]), the melt fraction will be ~ 0.5 vol.% (calculation details are given in the supporting information). Note that the secondary minerals in the slabs and ambient mantle including CaSiO_3 -perovskite, garnet, and stishovite may also contain large amounts of water (Chen et al., 2020; Katayama et al., 2003; Lin et al., 2020; Nisr et al., 2020). However, they have no phase transition when crossing 660-km depth. Their water contents should therefore remain nearly constant and not affect the melt fraction estimation in this study.

Although the dihedral angle of the bridgmanite + silicate melt system is unknown, it is expected to decrease with increasing pressure and estimated to be $< 10^\circ$ or nearly 0° at 660-km depth when extrapolated from the dihedral angle in the olivine-silicate melt system (Freitas & Manthilake, 2019). With such a low dihedral angle ($< 10^\circ$), 0.5–1.3 vol.% of melt is sufficient to completely wet the grain boundaries of bridgmanite, which will substantially affect the dynamics at the topmost lower mantle. For example, the melt may account for the seismic velocity reduction near 660-km depth (Schmandt et al., 2014). Another relevant example is viscosity. By complete wetting of grain boundaries, the viscosity of rocks could be significantly reduced by the pressure-solution creep mechanism, which may cause the topmost lower mantle to be rheologically much weaker (low viscosity) than the transition zone and deep lower mantle. Such a low-viscosity layer will largely prohibit whole mantle convection and may cause slab stagnation within the mantle transition zone (Fukao et al., 2009) because the resistance for horizontal flow is largely reduced (Mao & Zhong, 2018).

Data Availability Statement

The data sets for this research are given in Zenodo ([10.5281/zenodo.4288962](https://zenodo.org/record/4288962)).

Acknowledgments

The author appreciate the help of H. Fischer for high-pressure cell assembly preparation, R. Huang and D. Krauße for assistance in EPMA analysis, and R. Njål for sample polishing. Comments from two anonymous reviewers were helpful to improve the manuscript. This work is supported by the annual budget of the Bayerisches Geoinstitut. All of the SEM images for evaluation of this research are given in the supporting information.

References

- Bajgain, S., Ghosh, D. B., & Karki, B. B. (2015). Structure and density of basaltic melts at mantle conditions from first-principles simulations. *Nature Communications*, 6, 8578.
- Bolfan-Casanova, N., Keppler, H., & Rubie, D. C. (2000). Water partitioning between normally anhydrous minerals in the MgO-SiO₂-H₂O system up to 24 GPa: Implications for the distribution of water in the Earth's mantle. *Earth and Planetary Science Letters*, 182, 209–221.
- Chen, H., Leinenweber, K., Prakapenka, V., Prescher, C., Meng, Y., Bechtel, H., et al. (2020). Possible H₂O storage in the crystal structure of CaSiO₃ perovskite. *Physics of the Earth and Planetary Interiors*, 299, 106412.
- Dziewonski, A. M., & Anderson, D. L. (1981). Preliminary reference Earth model. *Physics of the Earth and Planetary Interiors*, 25, 297–356.
- Eugster, H. P. (1957). Heterogeneous reactions involving oxidation and reduction at high pressures and temperatures. *The Journal of Chemical Physics*, 26, 1760–1761.
- Fei, H., & Katsura, T. (2020). High water solubility of ringwoodite at mantle transition zone temperature. *Earth and Planetary Science Letters*, 531, 115987.
- Fei, H., Yamazaki, D., Sakurai, M., Miyajima, N., Ohfuji, H., Katsura, T., & Yamamoto, T. (2017). A nearly water-saturated mantle transition zone inferred from mineral viscosity. *Science Advances*, 3, e1603024.
- Freitas, D., & Manthilake, G. (2019). Electrical conductivity of hydrous silicate melts: Implications for the bottom-up hydration of Earth's upper mantle. *Earth and Planetary Science Letters*, 523, 115712.
- Fu, S., Yang, J., Karato, S. I., Vasiliev, A., Presniakov, M. Y., Gavriluk, A. G., et al. (2019). Water concentration in single-crystal (Al, Fe)-bearing bridgmanite grown from the hydrous melt: Implications for dehydration melting at the topmost lower mantle. *Geophysical Research Letters*, 46, 10346–10357. <https://doi.org/10.1029/2019GL084630>
- Fukao, Y., Obayashi, M., Nakakuki, T., & Deep Lab Project Group. (2009). Stagnant slab: A review. *Annual Review of Earth and Planetary Sciences*, 37, 19–46.
- Hernlund, J., Leinenweber, K., Locke, D., Tyburczy, J. A. (2006). A numerical model for steady-state temperature distributions in solid-medium high-pressure cell assemblies. *American Mineralogist*, 91, 295–305.
- Hirschmann M. M. (2006). Water, melting, and the deep Earth H₂O cycle. *Annual Review of Earth and Planetary Sciences*, 34, 629–653.
- Houser, C. (2016). Global seismic data reveal little water in the mantle transition zone. *Earth and Planetary Science Letters*, 448, 94–101.
- Ito, E., & Takahashi, E. (1987). Melting of peridotite at uppermost lower-mantle conditions. *Nature*, 328, 514–517.
- Katayama, I., Hirose, K., Yurimoto, H., & Nakashima, S. (2003). Water solubility in majoritic garnet in subducting oceanic crust. *Geophysical Research Letters*, 30, 2155. <https://doi.org/10.1029/2003GL018127>

- Katsura, T., Yoneda, A., Yamazaki, D., Yoshino, T., & Ito, E. (2010). Adiabatic temperature profile in the mantle. *Physics of the Earth and Planetary Interiors*, *183*, 212–218.
- Kelbert, A., Schultz, A., & Egbert, G. (2009). Global electromagnetic induction constraints on transition-zone water content variations. *Nature*, *460*, 1003–1006.
- Lin, Y., Hu, Q., Meng, Y., Walter, M., & Mao, H. K. (2020). Evidence for the stability of ultrahydrous stishovite in Earth's lower mantle. *Proceedings of the National Academy of Sciences of the United States of America*, *117*, 184–189.
- Litasov, K. D., Ohtani, E., Langenhorst, F., Yurimoto, H., Kubo, T., & Kondo, T. (2002). Water solubility in Mg-perovskites and water storage capacity in the lower mantle. *Earth and Planetary Science Letters*, *211*, 189–203.
- Litasov, K. D., Shatskiy, A., & Ohtani, E. (2013). Earth's mantle melting in the presence of C-O-H bearing fluid. In S. I. Karato (Ed.), *Physics and chemistry of the deep Earth* (pp. 38–65). John Wiley & Sons.
- Mao, W., & Zhong, S. (2018). Slab stagnation due to a reduced viscosity layer beneath the mantle transition zone. *Nature Geoscience*, *11*, 876–881.
- Matsukage, K. N., Jing, Z., & Karato, S. I. (2005). Density of hydrous silicate melt at the conditions of Earth's deep upper mantle. *Nature*, *438*, 488–491.
- Nakajima, A., Sakamaki, T., Kawazoe, T., & Suzuki, A. (2019). Hydrous magnesium-rich magma genesis at the top of the lower mantle. *Scientific Reports*, *9*, 7420.
- Nisr, C., Chen, H., Leinenweber, K., Chizmeshya, A., Prakapenka, V. B., Prescher, C., et al. (2020). Large H₂O solubility in dense silica and its implications for the interiors of water-rich planets. *Proceedings of the National Academy of Sciences of the United States of America*, *117*, 9747–9754.
- Ohtani, E., & Maeda, M. (2001). Density of basaltic melt at high pressure and stability of the melt at the base of the lower mantle. *Earth and Planetary Science Letters*, *193*, 69–75.
- Pearson, D. G., Brenker, F. E., Nestola, F., McNeil, J., Nasdala, L., Hutchison, M. T., et al. (2014). Hydrous mantle transition zone indicated by ringwoodite included within diamond. *Nature*, *507*, 221–224.
- Presnell, D. C. (1995). Phase diagrams of Earth-forming minerals. In T. J. Ahrens (Ed.), *Mineral physics & crystallography*. (pp. 248–268). American Geophysical Union. <https://doi.org/10.1029/RF002p0248>
- Sakamaki, T., Suzuki, A., & Ohtani, E. (2006). Stability of hydrous melt at the base of the Earth's upper mantle. *Nature*, *439*, 192–194.
- Sanloup, C., Drewitt, J. W. E., Konopkova, Z., Dalladay-Simpson, P., Morton, D. M., Rai, N., et al. (2013). Structural change in molten basalt at deep mantle conditions. *Nature*, *503*, 104–107.
- Schmandt, B., Jacobsen, S. D., Becker, T. W., Liu, Z., & Dueker, K. G. (2014). Dehydration melting at the top of the lower mantle. *Science*, *344*, 1265–1268.
- Shaw, H. R. (1963). Hydrogen-water vapor mixtures: Control of hydrothermal atmospheres by hydrogen osmosis. *Science*, *139*, 1220–1222.
- Suzuki, A., & Ohtani, E. (2003). Density of peridotite melts at high pressure. *Physics and Chemistry of Minerals*, *30*, 449–456.
- Suzuki, A., Ohtani, E., & Kato, T. (1995). Flotation of diamond in mantle melt at high pressure. *Science*, *269*, 216–218.
- Tan, E., Gurnis, M., & Han, L. (2002). Slabs in the lower mantle and their modulation of plume formation. *Geochemistry, Geophysics, Geosystems*, *3*, 1067. <https://doi.org/10.1029/2001GC000238>